

Chapter 2

IMAGING NEUROPEPTIDE RELEASE AT *DROSOPHILA* SYNAPSES WITH A GENETICALLY ENGINEERED REPORTER

Ding, K., Han, Y., Seid, T. W., Buser, C., Karigo, T., Zhang, S., Dickman, D. K., & Anderson, D. J. (2019). Imaging neuropeptide release at synapses with a genetically engineered reporter. *ELife*, 8. <https://doi.org/10.7554/elife.46421>

Han, Y., & Ding, K. (2022). Imaging Neuropeptide Release at *Drosophila* Neuromuscular Junction with a Genetically Engineered Neuropeptide Release Reporter. *Methods in Molecular Biology*, 2417, 193–203. https://doi.org/10.1007/978-1-0716-1916-2_15

Summary

Research on neuropeptide function has advanced rapidly, yet there is still no spatio-temporally resolved method to measure the release of neuropeptides *in vivo*. Here we introduce Neuropeptide Release Reporters (NPRRs): novel genetically-encoded sensors with high temporal resolution and genetic specificity. Using the *Drosophila* larval neuromuscular junction (NMJ) as a model, we provide evidence that NPRRs recapitulate the trafficking and packaging of native neuropeptides, and report stimulation-evoked neuropeptide release events as real-time changes in fluorescence intensity, with sub-second temporal resolution.

Introduction

Neuropeptides (NPs) exert an important but complex influence on neural function and behavior (Bargmann & Marder, 2013; Hokfelt et al., 2000; Insel & Young, 2000; Nassel & Winther, 2010). A major lacuna in the study of NPs is the lack of a method for imaging NP release *in vivo*, with subcellular spatial resolution and subsecond temporal resolution. Available techniques for measuring NP release include microdialysis (Kendrick, 1990), antibody-coated microprobes (Schaible, Jarrott, Hope, & Duggan, 1990), and GFP-tagged propeptides visualized either by standard fluorescence microscopy (van den Pol, 2012), or by TIRF imaging of cultured neurons (Xia, Lessmann, & Martin, 2009). In *Drosophila*, a fusion between rat Atrial Natriuretic Peptide/Factor (ANP/F) and GFP was used to investigate neuropeptide trafficking at the fly neuromuscular junction (NMJ) (Rao, Lang, Levitan, & Deitcher, 2001). Release was measured indirectly, as a decrease in ANP-GFP fluorescence intensity at nerve terminals reporting residual unreleased peptide, on a time-scale of seconds (Wong, Cavolo, & Levitan, 2015). None of these methods combined NP specificity, genetically addressable cell type-specificity, high temporal resolution and applicability to *in vivo* preparations (Supplementary Table 1). A major challenge is to develop a tool that encompasses all these features for direct, robust measurement of NP release *in vivo*.

Results

Neuropeptides are synthesized as precursors, sorted into dense core vesicles (DCVs), post-translationally modified and cleaved into active forms prior to release (Taghert & Veenstra, 2003). We reasoned that an optimal *in vivo* real-time NP release reporter should include (1) a reporter domain that reflects the physico-chemical contrast between the intravesicular milieu and the extracellular space (Figure 1—figure supplement 1A); and (2) a sorting domain that ensures its

selective trafficking into DCVs (Figure 1—figure supplement 1b). The NP precursor may function as the sorting domain, suggested by studies of DCV fusion using pIAPP-EGFP (Barg et al., 2002) and NPY-pHluorin (Zhu et al., 2007) in cultured neurons, or ANP-GFP in *Drosophila* (Rao et al., 2001). We therefore developed a pipeline to screen various transgenes comprising NP precursors fused at different sites to fluorescent reporters, in adult flies (Figure 1—figure supplement 1B-C). A total of 54 constructs were tested. We found that optimal trafficking was achieved by substituting the reporter for the NP precursor C-terminal domain that follows the final peptide (Figure 1—figure supplement 1B). In order to maintain covalent linkage with the reporter domain, we removed the dibasic cleavage site C-terminal to the final peptide.

The DCV lumen has lower pH and free calcium (pH = 5.5-6.75, $[Ca^{2+}] \sim 30 \mu M$) compared to the extracellular space (pH = 7.3, $[Ca^{2+}] \sim 2 mM$) (Mitchell et al., 2001; Sturman, Shakiryanova, Hewes, Deitcher, & Levitan, 2006). These differences prompted us to test validated sorting domains in a functional *ex vivo* screen using either pH-sensitive fluorescent proteins (Miesenbock, De Angelis, & Rothman, 1998) or genetically-encoded calcium indicators (GECIs) (Lin & Schnitzer, 2016; Tian, Hires, & Looger, 2012) (Figure 1—figure supplement 1A-D). Reporters based on pHluorins (Miesenbock et al., 1998) did not perform well in our hands, therefore we focused on GCaMP6s (Chen et al., 2013). The calcium sensitivity threshold of GCaMP6s is below the calcium concentration in both DCVs and the extracellular space. However, GCaMP6s fluorescence is quenched in the acidic DCV lumen (Barykina et al., 2016), enabling it to function as a dual calcium/pH indicator (Figure 1A). These key properties should boost the contrast between GCaMP6s fluorescence in unreleased vs. released DCVs, potentially allowing us to trace NP release at the cellular level *in vivo*.

We sought to test several NP precursor-GCaMP6s fusion proteins, called NPRRs (NeuroPeptide Release Reporters; unless otherwise indicated all NPRRs refer to fusions with GCaMP6s), in an intact preparation using electrical stimulation to evoke release. Initially for proof-of-principle experiments, we used the *Drosophila* larval NMJ to test NPRR^{ANP}, a GCaMP6s fusion with rat ANP (Burke et al., 1997). NMJ terminals are large, individually identifiable, and easy to image and record. In particular, boutons on muscle 12/13 are diverse—Type Ib and Type Is boutons contain mostly synaptic vesicles and few DCVs, while Type III boutons contain an abundance of DCVs but no synaptic vesicles (Menon, Carrillo, & Zinn, 2013); moreover, Type III-specific GAL4 drivers are available (Koon & Budnik, 2012) (Figure 1B).

Expression of NPRR^{ANP} pan-neuronally (under the control of *nsyb*-GAL4) followed by double immuno-staining for ANP and GCaMP (anti-GFP) indicated that the sorting domain and the reporter domains showed a similar localization in Type III neurons (Figure 1—figure supplement 2). Moreover, the distribution of NPRR^{ANP} overlapped that of Bursicon (Figure 1—figure supplement 3D), an NP that is endogenously expressed in Type III neurons (Loveall & Deitcher, 2010). Both GCaMP and Bursicon immunoreactivity were strongest within boutons, consistent with the known subcellular localization of DCVs (Gorczyca & Budnik, 2006).

Glutamate is the only known canonical neurotransmitter used at the larval NMJ (Menon et al., 2013). This allowed visualization of the subcellular localization of small synaptic vesicles (SV) by immuno-staining for vGluT, a vesicular glutamate transporter (Fremeau et al., 2001; Kempf et al., 2013). In Type Ib neurons (which contain relatively few DCVs relative to SVs (Menon et al., 2013)), vGluT

staining was observed as patches with dim center, which may reflect clustered SVs, while NPRR^{ANP} immunoreactivity was seen in dispersed, non-overlapping punctae (Figure 1C, α -GFP, inset). In Type III neurons, NPRRs were strongly expressed but no vGluT immunoreactivity was detected (Figure 1C). The subcellular distribution of this NPRR in larval NMJ neurons, therefore, is similar to that of other DCV-targeted markers previously used in this system (Rao et al., 2001; Shakiryanova, Tully, & Levitan, 2006), and appears to reflect exclusion from SVs.

The diffraction limit of light microscopy precluded definitive co-localization of NPRRs in DCVs. Therefore, we employed Immuno-Electron microscopy (Immuno-EM) to investigate the subcellular localization of NPRRs at the nanometer scale. To maximize antigenicity for Immuno-EM, we generated constructs that replaced GCaMP6s with GFP (NPRR^{ANP-GFP}); NPRR^{ANP-GFP} showed dense labeling in association with DCVs (Figure 1D, arrows), where the average number of gold particles/ μm^2 was substantially and significantly higher than in neighboring bouton cytoplasm (DCV/Bouton ~ 14.26) (Figure 1E, Supplementary Table 2). Taken together, these data indicate that NPRR^{ANP-GFP} is localized to DCVs. By extension, they suggest that NPRR^{ANP-GCaMP6s} (which has an identical structure to NPRR^{ANP-GFP} except for the modifications that confer calcium sensitivity) is similarly packaged in DCVs. While these two reporters show indistinguishable distributions by immunofluorescence, we cannot formally exclude that the substitution of GCaMP for GFP may subtly alter subcellular localization of the NPRR in a manner undetectable by light microscopy.

To measure the release of NPRRs from DCVs, we next expressed NPRR^{ANP} in Type III neurons using a specific GAL4 driver for these cells (Koon & Budnik, 2012) (Figure 2E and Figure 1—figure supplement 3D). We delivered 4 trials of 70 Hz electrical stimulation to the nerve bundle, a

frequency reported to trigger NP release as measured by ANF-GFP fluorescence decrease (Rao et al., 2001; Shakiryanova et al., 2006), and used an extracellular calcium concentration that promotes full fusion mode (Ales et al., 1999). This stimulation paradigm produced a relative increase in NPRR^{ANP} fluorescence intensity ($\Delta F/F$), whose peak magnitude increased across successive trials (Figure 2A, red bars and 2D; Video 1; Figure 2—figure supplement 1, A₁ vs. A₇). Responses in each trial showed a tri-phasic temporal pattern: (1) In the “rising” phase, NPRR^{ANP} $\Delta F/F$ peaked 0.5-5 secs after stimulation onset, in contrast to the virtually instantaneous peak seen in positive control specimens expressing conventional GCaMP6s in Type III neurons (Figure 2A-B). The NPRR^{ANP} latency to peak was similar to the reported DCV fusion latency following depolarization in hippocampal neurons (Xia et al., 2009). This delay is thought to reflect the kinetic difference between calcium influx and DCV exocytosis due to the loose association between DCVs and calcium channels (Xia et al., 2009). (2) In the “falling” phase, NPRR^{ANP} $\Delta F/F$ began to decline 1-5 seconds before the termination of each stimulation trial, presumably reflecting depletion of the available pool of releasable vesicles. In contrast, GCaMP6s fluorescence did not return to baseline until after stimulation offset (Figure 2A-B). (3) Finally, unlike GCaMP6s, NPRR^{ANP} exhibited an “undershoot” ($\Delta F/F$ below baseline) during the post-stimulation intervals, followed by a “recovery” phase (Figure 2A; Figure 2C, I1-4). This undershoot may reflect dilution of released fluorescent NPRR molecules by diffusion into the synaptic cleft (van den Pol, 2012), while recovery may reflect DCV replenishment in the boutons from vesicles proximal to the imaged release site.

Because NPRR^{ANP} fluorescence was preferentially accumulated within boutons, we asked whether these regions contributed to $\Delta F/F$ peaks more significantly than the inter-bouton intervals (IBIs). To do this, we partitioned the processes into boutons and IBI fields (Figure 2—figure supplement 2A), and compared the $\Delta F/F$ in these regions during stimulation trials. The time-averaged ratio of

bouton/IBI $\Delta F/F$ (see Materials and Methods) was significantly higher for NPRR^{ANP} than for GCaMP6s, particularly during later stimulation trials (Figure 2—figure supplement 2B, green bars, S2-4). This contrast indicates that NPRR^{ANP} signals are preferentially observed in boutons, where DCVs are located, and do not reflect differences in cytoplasmic free Ca²⁺ levels between these regions as detected by GCaMP6s.

To test definitively if NPRR^{ANP} $\Delta F/F$ signals are dependent upon NP release, we blocked vesicle fusion at terminals of Type III neurons using expression of tetanus toxin light chain (TNT) (Sweeney, Broadie, Keane, Niemann, & O'Kane, 1995), a protease that cleaves n-synaptobrevin, a v-snare required for DCV fusion (Figure 2—figure supplement 3) (T. Xu, Binz, Niemann, & Neher, 1998). As a control, we used impotent TNT (TNT^{imp}), a reduced activity variant (Sweeney et al., 1995). TNT expression completely abolished stimulation-induced $\Delta F/F$ increases from NPRR^{ANP}, while TNT^{imp} did not (Figure 2F). Further analysis revealed that both the $\Delta F/F$ peaks and inter-stimulation undershoots were diminished by TNT (Figure 2G-H). In contrast, neither TNT nor TNT^{imp} affected the kinetics of GCaMP6s signals in Type III neurons (Figure 2—figure supplement 2C), which report cytosolic Ca²⁺ influx. Taken together, these data support the idea that NPRR^{ANP} signals specifically reflect DCV release.

ANP is a rat NP that lacks a *Drosophila* homolog (Rao et al., 2001). To determine whether our method could be applied to detect the release of a specific, endogenous fly NP, we tested NPRR^{dTK}, one of 6 different reporter variants we initially generated from the *Drosophila* neuropeptide precursor, DTK (Figure 1—figure supplement 1B). In contrast to ANP which encodes a single peptide, DTK yields multiple NP derivatives (Winther, Siviter, Isaac, Predel, & Nassel, 2003). Light

microscopy (Figure 3A) and Immuno-EM (Figure 3B, arrows) confirmed that NPRR^{dTK}, like NPRR^{ANP}, was localized to DCVs (DCV/bouton ~22.19, Figure 3C). Using the Type III-specific GAL4 driver to express NPRR^{dTK} and the same stimulation protocol as used for NPRR^{ANP}, the basic tri-phasic response profile was also observed (Figure 3D). However, peak heights and baseline fluorescence fell progressively with successive stimulation trials (Figure 3E), in contrast to NPRR^{ANP} where the first peak and undershoot were lower (Figure 2C-D). The reason for this difference is currently unclear.

We next investigated the relationship between NPRR signal and stimulation intensity, by delivering to the Type III neurons a series of low to high frequency electrical stimuli (1-70 Hz; (Levitan, Lanni, & Shakiryanova, 2007)) while imaging the nerve terminals. For direct comparison of NPRR responses across different preparations, we applied *a posteriori normalization of fluorescent peaks in each trial to the highest response obtained among all trials*. For both NPRR^{ANP} and NPRR^{dTK} (Figure 4A-B), the peak responses showed a positive correlation with stimulation frequency, analogous to that observed using cytosolic GCaMP6s (Figure 4C). In Type III neurons, the responses of both NPRRs to stimulation frequencies <30 Hz (1,5,10,20 Hz) were not statistically significant from zero. NPRR^{ANP} showed a higher sensitivity to high stimulation frequencies (30 Hz: 18.14%, 50 Hz: 82.40% Normalized peak $\Delta F/F$), while NPRR^{dTK} showed a higher stimulation threshold and lower sensitivity (30Hz: 3.57%, 50Hz: 24.67% Normalized peak $\Delta F/F$).

We next investigated whether the relatively high stimulation frequency required to observe significant responses with NPRRs was a function of the reporters, or rather of the cell class in which they were tested. To do this, we expressed both NPRRs in Type Ib neurons, a class of motor neurons

that contains both SVs and DCVs (Figure 1B, Figure 4D-F), and performed stimulation frequency titration experiments. Strikingly, in Type Ib neurons, significant increases in $\Delta F/F$ could be observed at frequencies as low as 10 Hz (Figure 4D, E; NPRR^{ANP} @ 20 Hz: 12.50%, NPRR^{dTK} @ 20 Hz: 17.67% normalized peak $\Delta F/F$). The reason for the difference in NPRR threshold between Type III and Type Ib neurons is unknown, but parallels their difference in GCaMP6s response to electrical stimulation (Figure. 4C vs. 4F).

Notably, although NPRR^{ANP} and NPRR^{dTK} presented distinct response profiles in Type III neurons, their performance in Type Ib neurons was more similar (Fig. 4A vs. 4B; cf. 4D vs. 4E). In summary, the differences in performance we observed between the two NPRRs appeared to be specific to Type III neurons, and were minor in comparison to the differences in performance of both reporters between the two cell classes in. The reason for the differences between NPRR^{ANP} and NPRR^{dTK} sensitivity and kinetics in Type III neurons is unknown but may reflect differences in how well these reporters compete with the high levels of endogenous neuropeptide (Bursicon) for packaging, transport or release.

Discussion

Here we present proof-of-principle for a method to detect the release of different neuropeptides in intact neural tissue, with subcellular spatial and sub-second temporal resolution. By exploiting the fluorescent change of GCaMP in response to a shift in pH and $[Ca^{2+}]$, we visualized the release of neuropeptides by capturing the difference between the intravesicular and extracellular microenvironment. NPRR responses exhibited triphasic kinetics, including rising, falling and recovery phases. In the falling phase, a post-stimulus “undershoot,” was observed in which the

fluorescent intensity fell below pre-stimulation baseline. This undershoot presumably reflects the slow kinetics of DCV replenishment relative to release.

The molecular mechanisms of NP release are incompletely understood (Tao Xu & Xu, 2008). It is possible that individual DCVs only unload part of their cargo during stimulation, in which case many DCVs that underwent fusion may still contain unreleased NPRR molecules following a stimulus pulse. Although we are convinced that NPRR signals do indeed reflect NP release, due to the presence of the recovery phase, we cannot formally exclude that unreleased NPRRs may contribute to the signal change due to their experience of intravesicular $[Ca^{2+}]$ /pH changes that occur during stimulation. To resolve this issue in the future, an ideal experiment would be to co-express an NPRR together with a $[Ca^{2+}]$ /pH-invariant NP-reporter fusion. Multiple attempts to generate such fusions with RFP were unsuccessful, due to cryptic proteolytic cleavage sites in the protein which presumably result in degradation by DCV proteases during packaging.

To test if $NPRR^{ANP} \Delta F/F$ signals are dependent on NP release, we expressed the light chain of tetanus toxin (TNT), a reagent shown to effectively block NP release in many (Hentze, Carlsson, Kondo, Nassel, & Rewitz, 2015; McNabb & Truman, 2008; Zandawala et al., 2018), if not all (Umezaki, Yasuyama, Nakagoshi, & Tomioka, 2011), systems. We observed a striking difference in NPRR kinetics in flies co-expressing TNT vs. its proteolytically inactive “impotent” control form TNT^{imp} (Figure 2F). The strong reduction of NPRR signals by TNT-mediated n-syb cleavage is consistent with the idea that these signals reflect the release of NPRRs from DCVs.

We have tested the generalizability of the principles used to generate NPRRs by (1) constructing a surrogate NP reporter NPRR^{ANP} as well as a multi-peptide-producing endogenous *Drosophila* NP reporter NPRR^{dTK} (Figure 2-3); (2) characterized NPRR signals in response to varying intensities of electrical stimulation; and (3) recorded NPRR signals in two different classes of NMJ motor neurons containing DCVs with or without SVs, respectively (Figure 4). These experiments revealed, to our surprise, that NPRR responses exhibit cell-type specific characteristics (Figure 4). As NPRRs are applied to other neuropeptides and cell types, a systematic characterization of neuropeptide release properties in different peptidergic neurons should become possible, furthering our understanding of neuropeptide biology.

The method described here can, in principle, be extended to an *in vivo* setting. This would open the possibility of addressing several important unresolved issues in the study of NP function *in vivo*. These include the “which” problem (which neuron(s) release(s) NPs under particular behavioral conditions?); the “when” problem (when do these neurons release NPs relative to a particular behavior or physiological event?); the “where” problem (are NPs released from axons, dendrites or both?); and the “how” problem (how is NP release regulated?). The application of NPRRs to measuring NP release dynamics in awake, freely behaving animals may yield answers to these important long-standing questions.

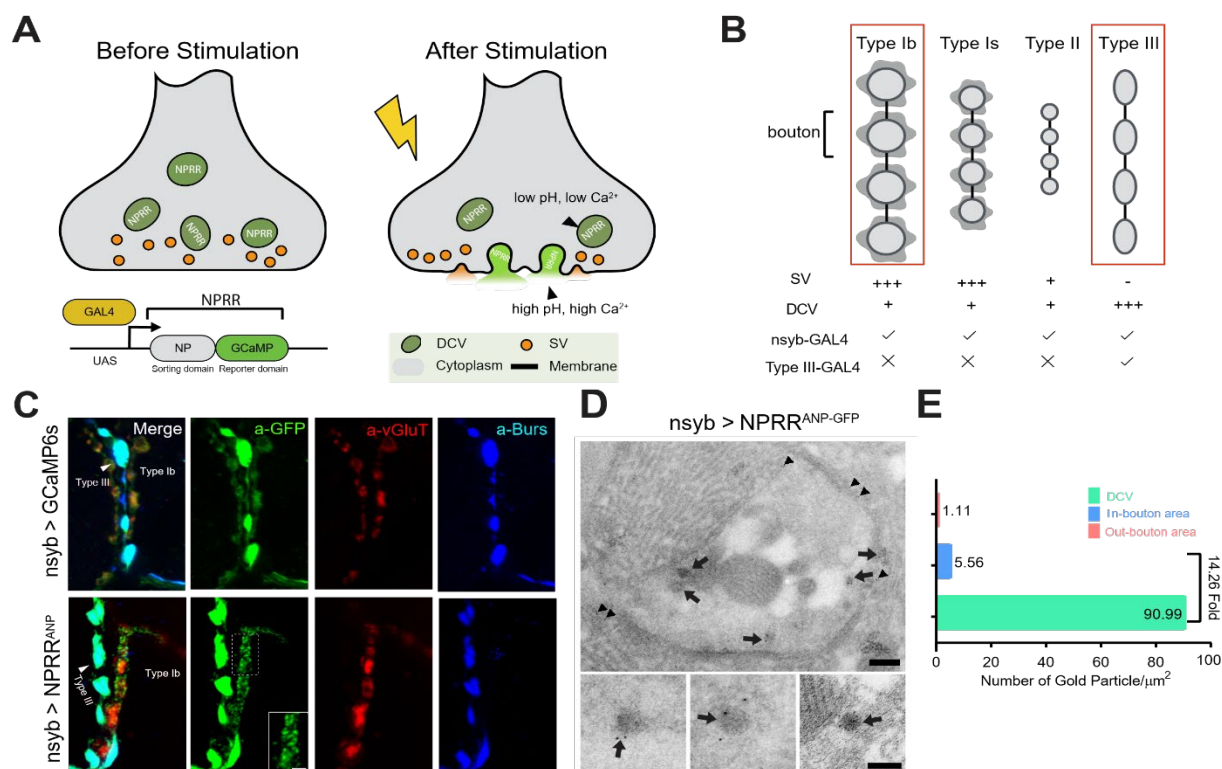


Figure 1: Localization of an NPRR.

(A) Schematic illustrating the principle of NPRRs (Neuropeptide Release Reporters). NPRR molecules in the DCV lumen (low pH/low calcium, *left*) exhibit increased fluorescence when released by fusion into the extracellular space (neutral pH/high calcium, *right*). NPRR fluorescent signal is expected to decay following diffusion into the synaptic cleft. New NPRR-containing DCVs are produced by synthesis and transport from the soma, not by recycling. NP: Neuropeptide. DCV: Dense Core Vesicle. SV: Synaptic Vesicle. (B) Distinct motor neuron subtypes at the *Drosophila* NMJ (muscle 12/13) have different proportions of DCVs vs. SVs. The GAL4 driver R57C10-Gal4 (nsyb-GAL4) labels all subtypes, while R20C11-GAL4 selectively labels only Type III neurons, which lack SVs (“Type III-GAL4”). Light grey circles, black lines and dark grey shading represent boutons, inter-bouton intervals and subsynaptic reticulum, respectively. The studies in this paper focus on Type Ib neurons and Type III neurons (in red rectangles). (C) Triple immunolabeling for GFP (green), Bursicon (blue) and vGluT (red), in flies containing nsyb-GAL4 driving UAS-GCaMP6s (*upper*), or NPRR^{ANP} (*lower*). Type Ib and Type III boutons are indicated. Scale bar, 5 μm . Inset image (NPRR^{ANP}, a-GFP channel) shows details of puncta distribution of NPRR^{ANP} in Type Ib neuron. Scale bar, 2 μm . (D) TEM images of boutons immunolabeled with anti-GFP (5 nm gold particle-conjugated) to detect nsyb>NPRR^{ANP}-GFP, which has an identical structure to NPRR^{ANP}, but is a GFP rather than GCaMP6s fusion to improve antigenicity. Note strong labeling in DCVs (arrows) and the neuronal plasma membrane (arrowheads). Scale bar, 200 nm. Lower panel shows representative images of labeled DCVs. Scale bar, 100 nm. (E) Quantification for TEM images in (D).

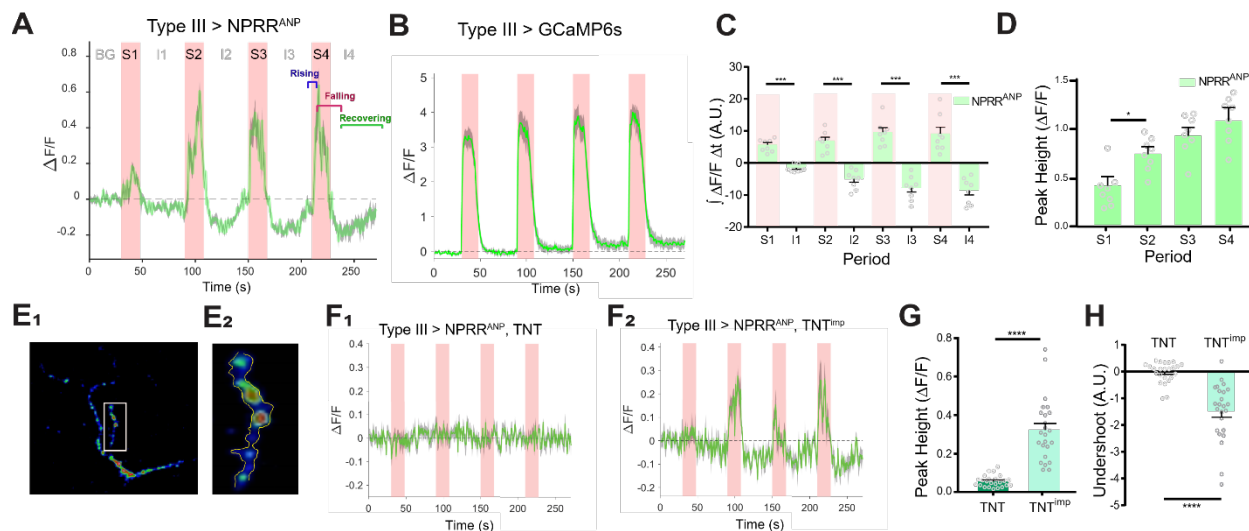


Figure 2: NPRR specifically reports neuropeptide release.

(A) Trace from a representative experiment showing changes in NPRR^{ANP} fluorescence intensity ($\Delta F/F$) in Type III motor neurons at the larval NMJ evoked by electrical stimulation. BG: background. S1-S4: Stimulation trials 1-4. I1-I4: Inter-stimulation Intervals (ISIs) 1-4. Green line: $\Delta F/F$ averaged across all boutons in the field of view. Grey shading: s.e.m envelope. Red bar: electrical stimulation trials (70 Hz). The three typical phases of the response are indicated in S4. The peak height of the response on the first trial is characteristically lower (see also (D)), and may reflect competition with unlabeled DCVs in the readily releasable pool. (B) $\Delta F/F$ traces in control flies expressing cytoplasmic GCaMP6s in Type III neurons. (C) Integrated NPRR^{ANP} $\Delta F/F$ values during trials S1-4 and intervals I1-4. A.U.: arbitrary units. $n = 8$. ***, $P < 0.001$. (D) Average NPRR^{ANP} $\Delta F/F$ peak heights for trials S1-4. $n = 8$. *, $P < 0.05$. Plotted values in (C-D) are mean \pm s.e.m. (E1-E2) Representative selection of ROIs (yellow). Details see **Materials and methods**. Scale bar, 5 μ m. (F) NPRR^{ANP} $\Delta F/F$ response are abolished in Type III GAL4>UAS-NPRR^{ANP} flies bearing UAS-TNT (F1) but not UAS-TNT^{imp} (F2). (G) Average peak heights of NPRR^{ANP} $\Delta F/F$ in combined stimulation trials (S1-4) from (F). ****, $P < 0.0001$. (H) Average “undershoot,” defined as the integrated $\Delta F/F$ during ISIs I1-4 (see (C)). In C-D and G-H.

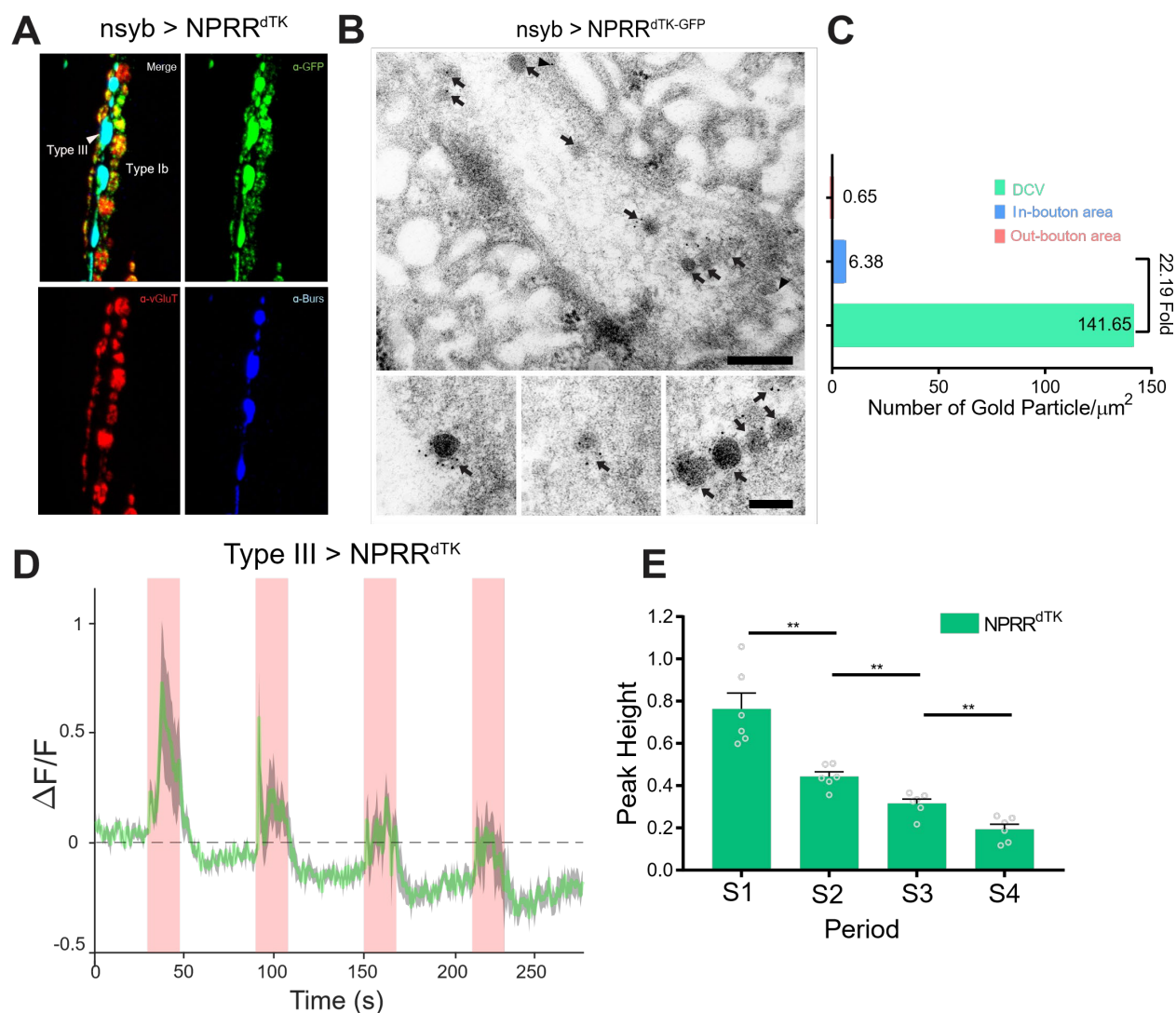


Figure 3: Application of the NPRR approach to a *Drosophila* neuropeptide.

(A) Triple immunolabeling for GFP (green), Bursicon (blue) and vGluT (red) in Type III-GAL4>UAS-NPRR^{dTK} flies. Scale bar, 5 μm. **(B)** TEM images of boutons immunolabeled against GFP (5 nm gold) in nsyb-GAL4>UAS-NPRR^{dTK-GFP} flies. Note strong labeling in DCVs (arrows) and bouton plasma membrane (arrowheads). Scale bar, 200 nm. Lower panel shows representative images of labeled DCVs. Scale bar, 100 nm. **(C)** Quantification of TEM images in **(B)**. **(D)** NPRR^{dTK} ΔF/F curve; stimulation conditions as in **Figure 2A**. **(E)** Average NPRR^{dTK} ΔF/F peak height above pre-stimulation baseline (corrected; see **Materials and methods**) for stimulation trials S1-4. $n = 6$. **, $P < 0.01$.

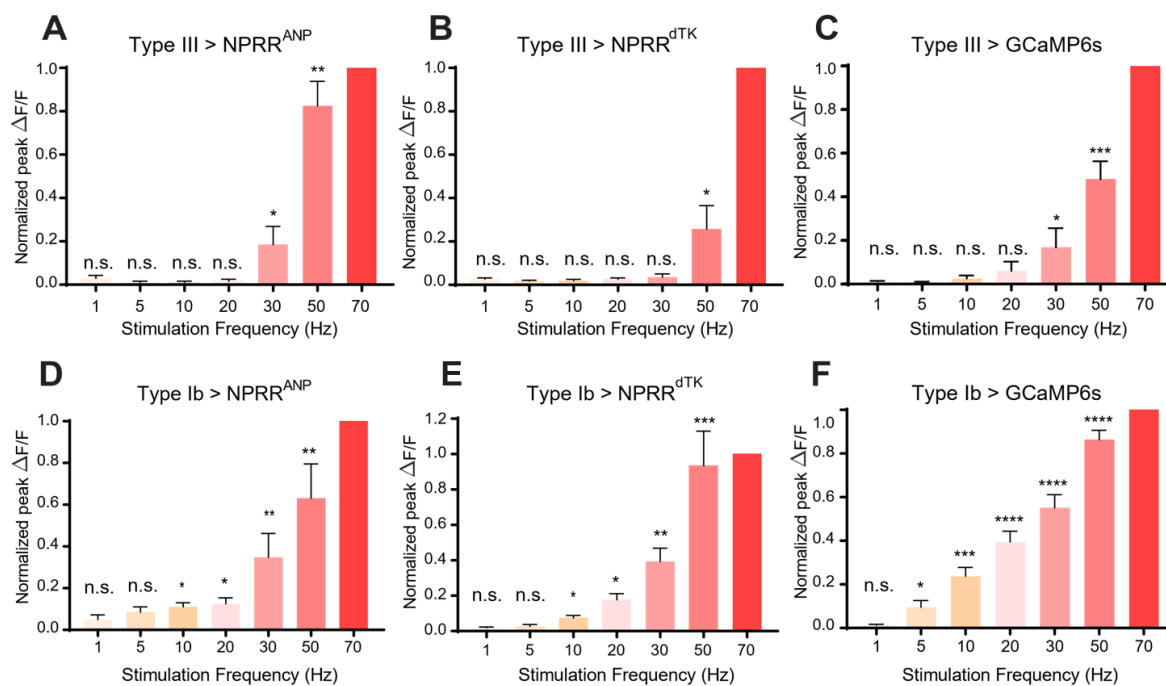


Figure 4: NPRR reveals distinct cell-type specific peptide release properties.

For each preparation, a series of stimulation trials were delivered at frequencies from 1 Hz to 70 Hz, as indicated. In-stimulation response peaks were normalized to 70 Hz. The normalized peaks of NPRRs or calcium responses (measured with cytosolic GCaMP6s) were pooled and plotted for both Type III (**Figure 4A-C**) and Type Ib (**Figure 4D-F**) neurons. Responses were compared to zero. $n = 6-12$. n.s., not significant. *, $P < 0.05$. **, $P < 0.01$. ***, $P < 0.001$. ****, $P < 0.0001$.

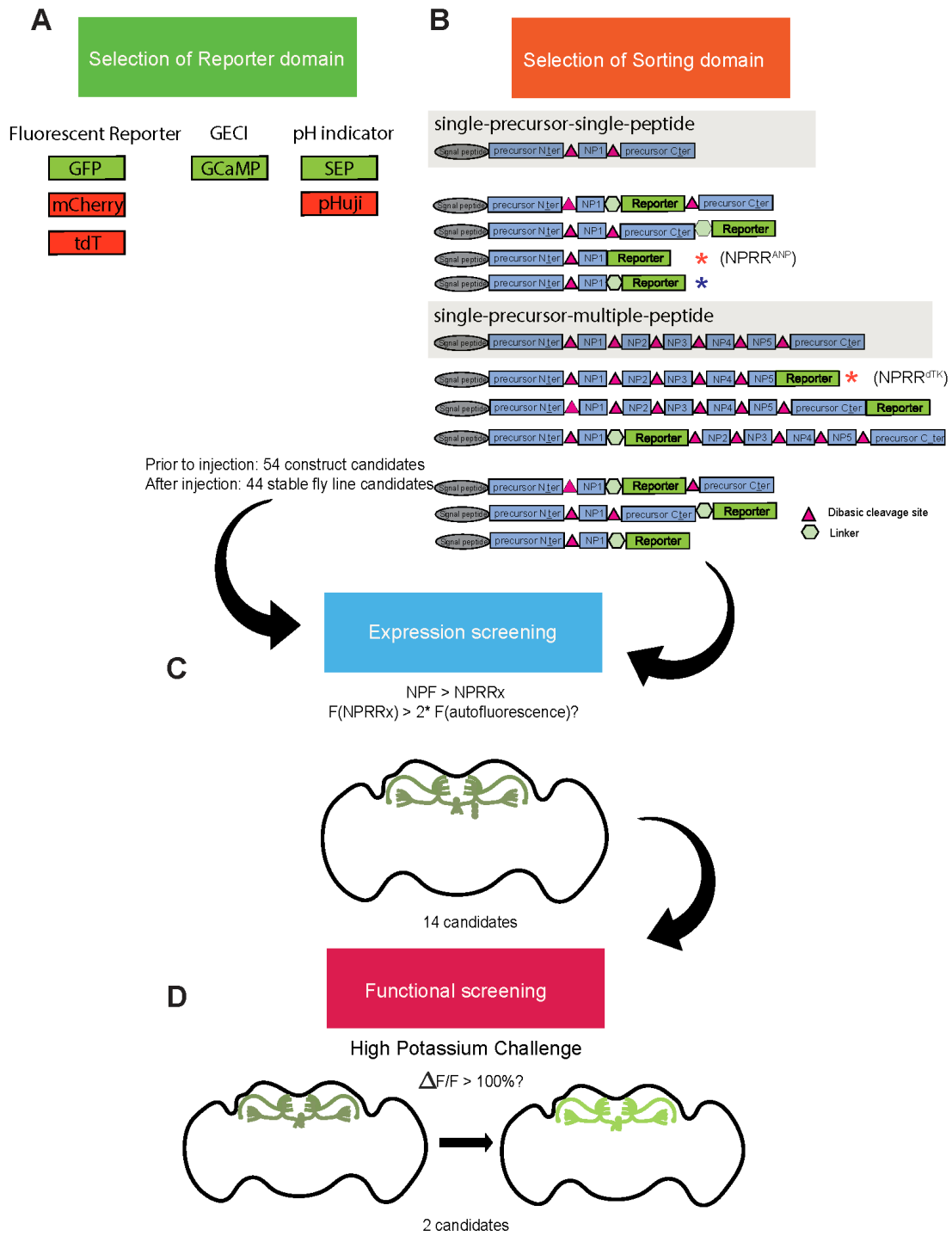


Figure 1—figure supplement 1: NPRR screening pipeline.

A series of reporter-neuropeptide precursor fusions were designed, codon-optimized for *Drosophila*, cloned into expression vectors under the control of the GAL4 upstream activator sequence (UAS), and used to generate transgenic flies. **(A)** Candidate reporters interrogated included (constitutive) fluorescent reporters, genetically encoded calcium indicators (GECI) and pH indicators (pHluorins). **(B)** Sorting domain candidates included different truncated versions of rat Atrial Natriuretic Peptide (ANP; single-precursor-single-peptide) and *Drosophila* tachykinin (dTK; single-precursor-multiple-peptide) precursors. 52 constructs were built and injected. 44 of 54 were successfully integrated as transgenic lines, while 8 were excluded due to lethality or unstable expression. **(C-D)** Candidate UAS-NPRR lines were crossed with an NPF-Gal4 driver line and selected based on their expression in NPF terminals in the adult fly brain. The raw fluorescence intensity of each NPRR candidate was measured using the same microscope parameters (laser power, HV, offset value). 14 candidates passed this screening. **(C)** We screened the performance of difference NPRRs (signal-to-noise contrast) by measuring fluorescence before and immediately after 70mM high-potassium challenge in an *ex vivo* explant preparation of adult fly brains. The post/pre KCl fluorescence ratio is defined as $\Delta F/F$. We arbitrarily set the threshold as 100%. 2 NPRRs with highest $\Delta F/F$ passed the final round of screening.

Red asterisks indicate the candidates selected for the studies in **Figure 2** and **Figure 3**. Blue asterisk indicates original ANP-GFP fusion)(Burke et al., 1997; Rao et al., 2001).

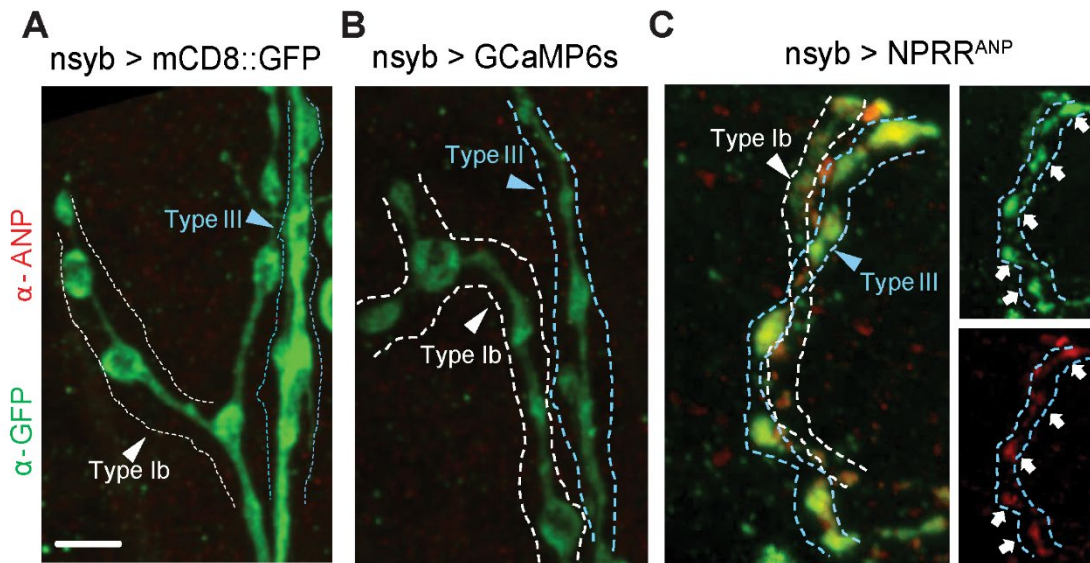


Figure 1—figure supplement 2: Exogenous neuropeptide ANP dictates the expression pattern of NPRR^{ANP}.

Membrane-bound mCD8::GFP fusion (A), cytosolic GCaMP6s (B) and NPRR^{ANP} (C) were expressed pan-neuronally in the larval NMJ and stained for both ANP (red) and NPRR (green, anti-GFP). (C) Note co-localization of ANP and GFP. Scale bar, 5 μ m.

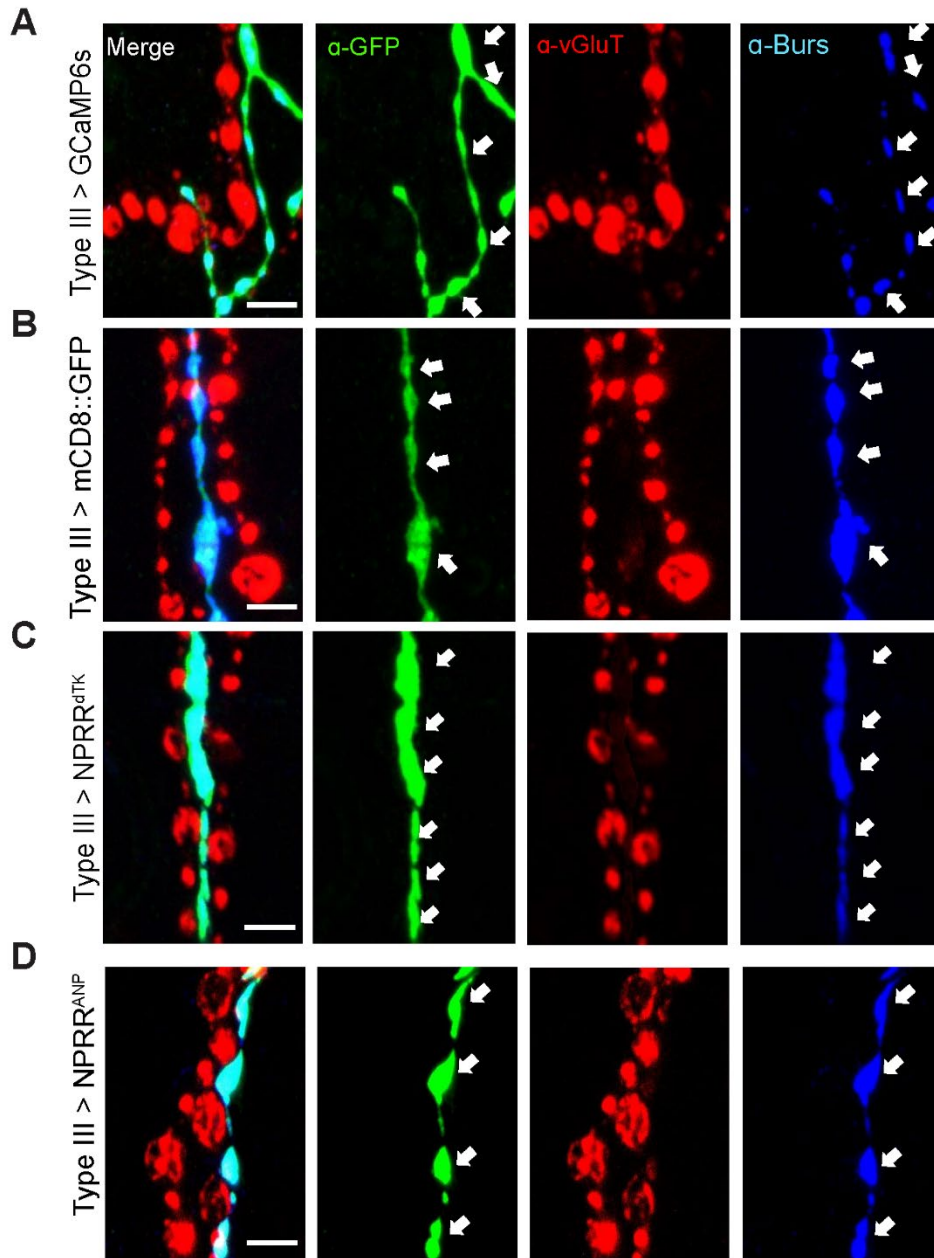


Figure 1—figure supplement 3: Expression of different reporters in Type III neurons in the larval NMJ.

A GAL4 line (R20C11-GAL4, named Type III-GAL4 in this report) allows specific expression in Type III neurons. Expression patterns of (A) conventional GCaMP, (B) membrane-bound GFP, (C) NPRR^{dTK} and (D) NPRR^{ANP} using Type III-GAL4. Arrows indicate boutons in Type III neurons, which contain the neuropeptide Bursicon. Note that anti-vGluT stains other types of motor neurons, which are not labeled by the Type III-specific driver used in this experiment. Scale bar, 5 μ m.

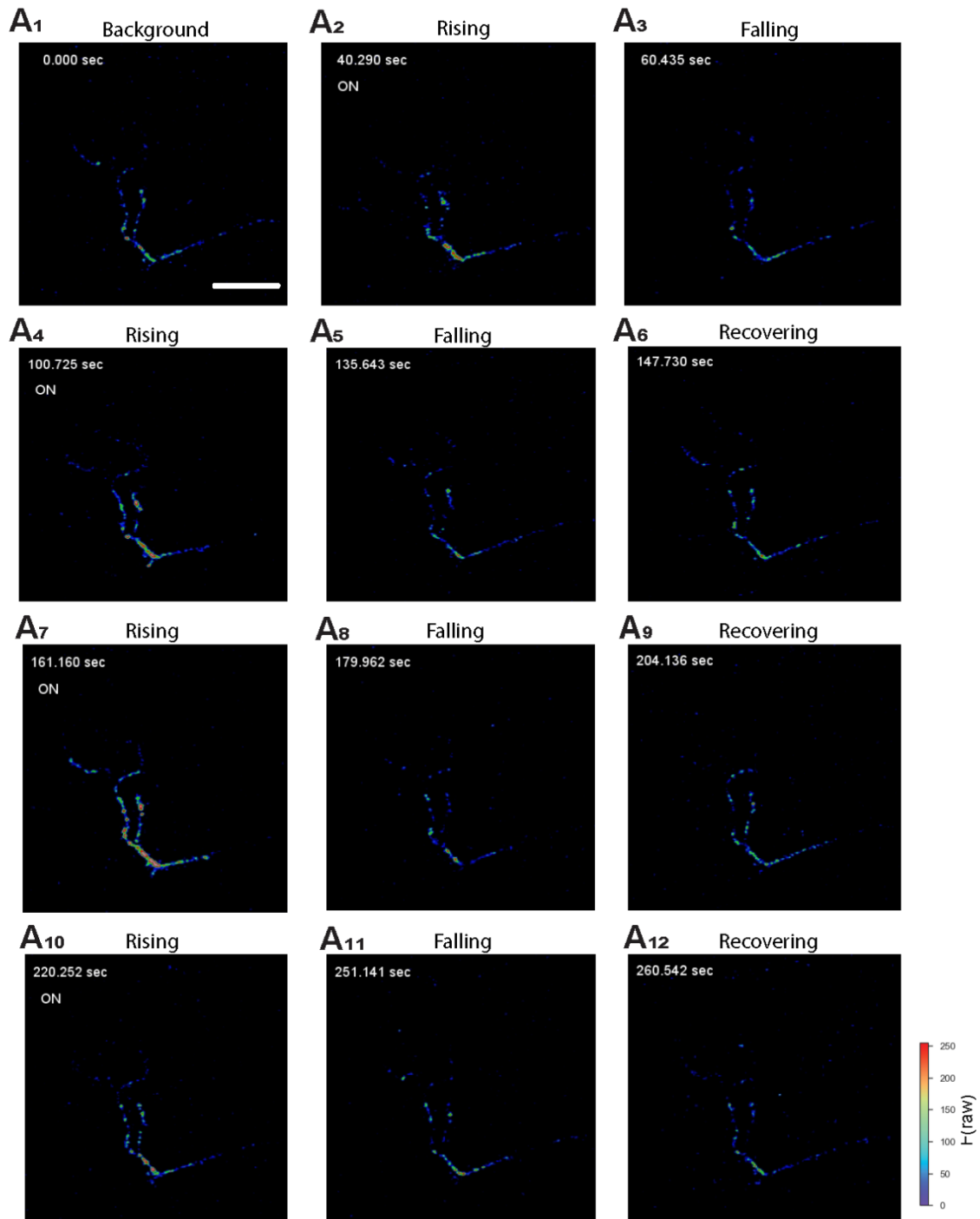


Figure 2—figure supplement 1: Activation of NPRR^{ANP} *in situ*.

Representative still frames (A₁-A₁₂) from video recordings of NPRR^{ANP}-expressing Type III neurons at the larval NMJ. “On” (A_{2,4,7,10}) represents the onset of electrical pulses. Color bar: Raw fluorescence intensity. Scale bar, 50 μ m.

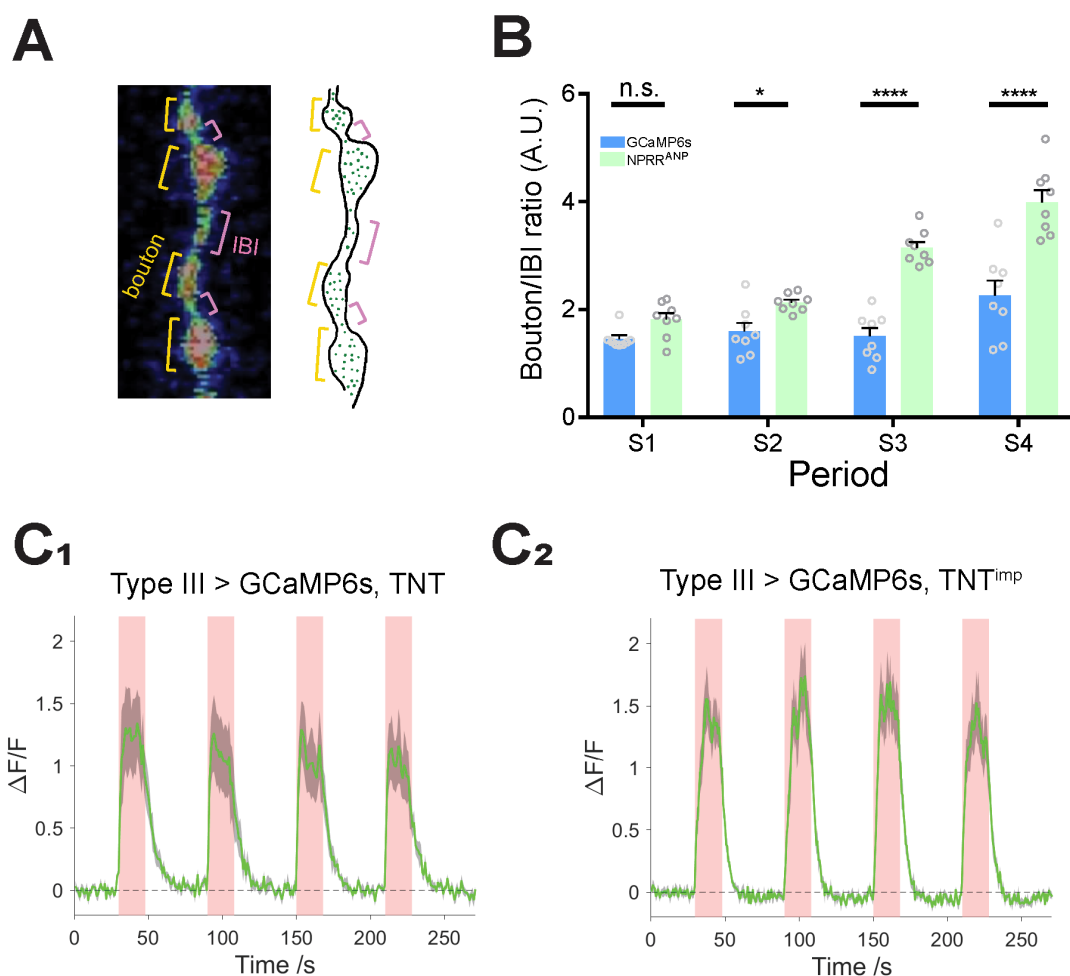


Figure 2—figure supplement 2: NPRR specifically reports neuropeptide release.

(A) Left: Segmentation of Type III neurons into boutons (orange) and inter-bouton intervals (IBIs, red). Right: Schematic illustrating DCV distribution in Type III neurons, based on photomicrograph to the left. Green dots, DCVs. **(B)** Average time-integrated ratio of $\Delta F/F$ in boutons/IBIs (**Materials and Methods**), within each stimulation periods. n.s., not significant. *, $P < 0.05$. ***, $P < 0.001$. ****, $P < 0.0001$. **(C)** TNT does not affect GCaMP6s $\Delta F/F$ kinetics. $n = 6-7$. GCaMP6s peak magnitudes were reduced slightly in TNT (**C₁**) in comparison to TNT^{imp} (**C₂**) preparations, perhaps reflecting partial vulnerability of the cytosolic GCaMP6s reporter to TNT-mediated cleavage and degradation. NPRRs are expected to be protected from TNT by the DCV membrane.

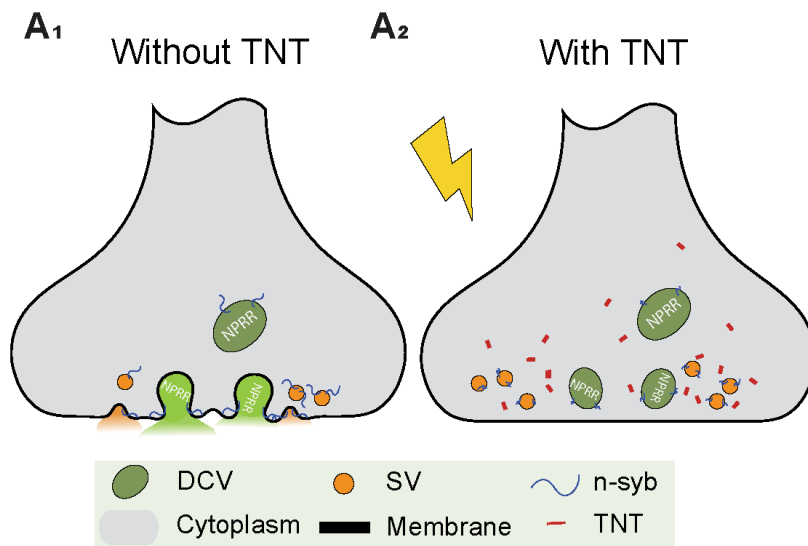


Figure 2—figure supplement 3: Blocking DCV fusion using Tetanus Toxin.
(A₁, A₂) Tetanus toxin (TNT) blocks vesicle fusion by cleavage of n-synaptobrevin (n-syb).

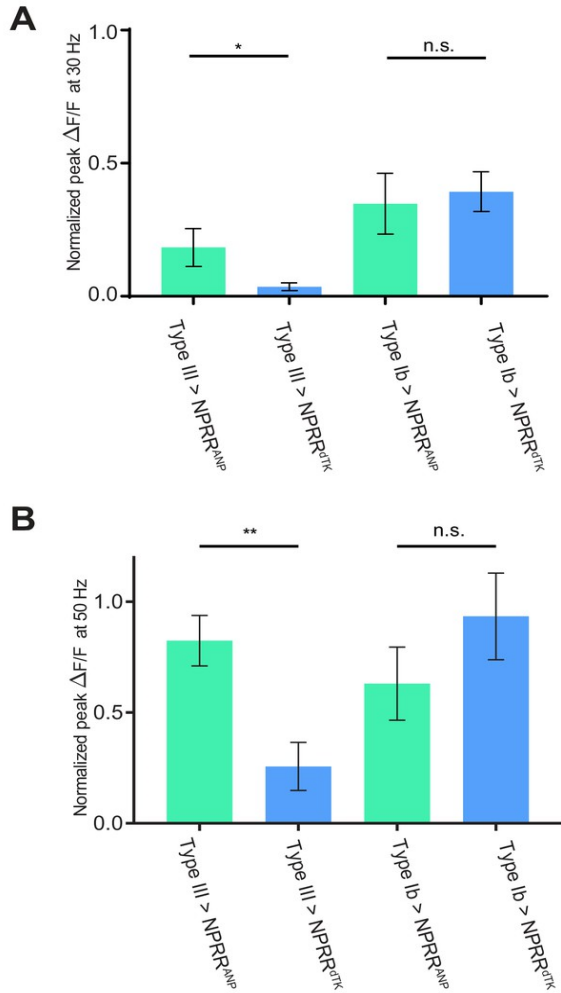


Figure 4—figure supplement 1: Comparison of NPRR response at 30 and 50 Hz.

Normalized $\Delta F/F$ peaks in at 30 Hz (**A**) and 50 Hz (**B**) electrical stimulation in Figure 4A, B, D, E are replotted and compared. $n = 6-7$. *, $P < 0.05$. **, $P < 0.01$. n.s., not significant.

Current techniques for neuropeptide release measurement

	Chemical specificity	Genetic specificity	Spatial specificity	Temporal dynamics	Signal relative to background
Microdialysis	Low	NA	Brain region	minutes-days	High
Antibody-coated microprobe	High	NA	Brain region	minutes-days	High
GFP-tagged propeptide imaging	High	Yes	Neuron of interest	~seconds	Low
NPRR	High	Yes	Neuron of interest	~subseconds	High

Supplementary Table. 1: Current techniques for neuropeptide release measurement.

Summary of current techniques used for neuropeptide release, including microdialysis, antibody-coated microprobes, GFP-tagged propeptide imaging and NPRR. NA, “not applicable”

	NPRR ^{ANP-GFP} (Ib)	NPRR ^{dTK-GFP}
average gold particles per DCV	0.71	1.11
gold within DCV area [μm^{-2}]	90.99	141.65
gold within bouton area [μm^{-2}]	5.56	6.38
gold outside bouton area [μm^{-2}]	1.11	0.65
controls		
gold per imaged area [μm^{-2}]	2.18	2.47
background (internal control) [μm^{-2}]	0.57	0.52
background (biological control) [μm^{-2}]	0.25	-
SNR (gold/DCV area vs. background)	159.6	272.4

Supplementary Table. 2: Stereological labeling estimates

Stereological labeling estimations of NPRR^{ANP-GFP} and NPRR^{dTK-GFP}, respectively, in Type Ib neurons, or in Type Ib and Type III neurons. Biological controls and internal controls are described in Materials and methods. SNR: Signal-to-Noise Ratio.

Key Resources Table

Reagent type (species) or resource	Designation	Source or reference	Identifiers	Additional information
Genetic reagent (<i>D. melanogaster</i>)	UAS-NPRR ^{ANP} (attp2)	this paper		See Materials and methods, subsection Construction of transgenic animals.
Genetic reagent (<i>D. melanogaster</i>)	UAS-NPRR ^{dTK} (attp2)	this paper		Same as above.
Genetic reagent (<i>D. melanogaster</i>)	UAS-TNT ^{imp}	Bloomington Drosophila Stock Center	BDSC:28840; FLYB:FBti0038575; RRID:BDSC_28840	Flybase symbol: w[*]; P{w[+mC]=UAS TeTxLC. (-)V}A2
Genetic reagent (<i>D. melanogaster</i>)	UAS-TNT	Bloomington Drosophila Stock Center	BDSC:28838; FLYB:FBti0038527; RRID:BDSC_28838	Flybase symbol: w[*]; P{w[+mC]=UAS TeTxLC.tnt}G2
Genetic reagent (<i>D. melanogaster</i>)	w; +; UAS-GCaMP6s (su(Hw)attp1)	Hoopfer et al., 2015		
Antibody	anti-GFP (chicken polyclonal)	Aveslab	Aveslab: GFP-1020; RRID:AB_2307313	(1:250:Immuno-EM, 1:1000: IHC)
Antibody	anti-ANP (rabbit polyclonal)	abcam	abcam #14348	(1:500)

Materials and Methods

Fly strains

All experimental flies were reared on a 12/12-hour day-night cycle at 25°C. Standard chromosomal balancers and genetic strategies were used for all crosses and for maintaining mutant lines. The following strains were obtained from Bloomington Stock Center (Indiana University): R20C11-Gal4 (#48887), R57C10-Gal4 (#39171), UAS-mCD8::GFP (#32185), UAS-TNT (#28838), UAS-TNT^{imp} (#28840). UAS-opGCaMP6s was made by Barret Pfeiffer (Gerald Rubin's lab, Janelia Farm) (Hoopfer, Jung, Inagaki, Rubin, & Anderson, 2015).

Construction of transgenic animals

All PCR reactions were performed using PrimeSTAR HS DNA polymerase (Takara #R045Q). All constructs were verified via DNA sequencing (Laragen).

To construct UAS-NPRR^{ANP}, *Drosophila* codon-optimized ANP and GCaMP6s were synthesized using gBlocks service (Integrated DNA Technologies), and subcloned into pJFRC7 vector (from Addgene #26220)(Pfeiffer et al., 2010) using Gibson cloning. UAS-dTK-NPRR is built in a similar way except the dTK fragment was cloned from the *Drosophila* brain cDNA. NPRRdTK-GFP and NPRRANP-GFP were built similarly except *Drosophila* codon-optimized GFP was used for the subcloning. All the vectors were injected and integrated into attP2 or attP40 sites (Bestgene Inc).

Expression screening of NPRR candidates

Adult fly brains were dissected in chilled PBS and fixed in 4 % formaldehyde for 55 min at room temperature. After three 10 min rinses with PBS, the brains were cleared with Vectashield (#1000, Vectorlabs), mounted, and used for native fluorescence measurements. We trace the NPF neuron somata and arborization as ROIs. We selected regions next to NPF neurons and measured its fluorescent intensity as a reference, which represents background autofluorescence. Candidates whose fluorescence reached at least 2-fold higher than reference were selected for functional screening.

Functional screening of NPRR candidates

For the baseline fluorescence measurement, we crossed NPF-Gal4 to the candidate lines and generated NPF-Gal4 > NPRRx (x = candidate label) flies for tests. The dissected adult fly brains were mounted on a petri dish and immersed in *Drosophila* imaging saline (108 mM NaCl, 5 mM KCl, 2 mM CaCl₂, 8.2 mM MgCl₂, 4 mM NaHCO₃, 1 mM NaH₂PO₄, 5 mM trehalose, 10 mM sucrose, 5 mM HEPES, pH 7.5). To deliver high potassium challenge, High-K imaging saline was perfused (43 mM NaCl, 70 mM KCl, 2 mM CaCl₂, 8.2 mM MgCl₂, 4 mM NaHCO₃, 1 mM NaH₂PO₄, 5 mM trehalose, 10 mM sucrose, 5 mM HEPES, pH 7.5). Live imaging series were acquired using a Fluoview FV3000 Confocal laser scanning biological microscope (Olympus) with a 40×, 0.8 N.A. (Numerical Aperture) water immersion objective (Olympus). Candidates whose post-stimulation fluorescence reached at least 2-fold of baseline fluorescence (measured as averaged pre-stimulation fluorescence) were selected for *in vivo* tests at NMJ. For each candidate line, at least 3 brains were tested and fold-change of each was averaged.

Immunocytochemistry (ICC)

Cells were fixed in 4 % formaldehyde or Bouin's solution for 30 min at room temperature. After three 15 min rinses with PBS, tissues were incubated with primary antibodies overnight at 4 °C. Following three 15 min rinses with PBS, tissues were incubated with secondary antibody for 2 hours at room temperature. Following three 15 min rinses, tissues were cleared with Vectashield (#1000, Vectorlabs) and mounted. Confocal serial optical sections were acquired using a Fluoview FV3000 Confocal laser scanning biological microscope (Olympus) with a 60×, 1.30 N.A. silicone oil objective (Olympus). All image processing and analyses were done using ImageJ (National Institute of Health).

The following primary antibodies were used: Chicken anti-GFP (1:250-1:1000, Aveslab #1020), Rabbit anti-ANP (1:500, abcam #14348), Guinea pig anti-vGluT(Goel & Dickman, 2018) (1:1500), Rabbit anti-syt1(Littleton, Bellen, & Perin, 1993) (1:500) and Rabbit anti-Bursicon (1:2000, a gift from Dr. Benjamin White).

The following secondary antibodies were used: Alexa Fluor 488 Goat anti-Chicken IgY (#A11039, Invitrogen), Alexa Fluor 488 Goat anti-Rabbit IgG (#A11008, Invitrogen), Alexa Fluor 568 Goat anti-Rabbit IgG(H+L) (#A11011, Invitrogen), Alexa Fluor 633 Goat anti-Rabbit IgG(H+L) (#A21070, Invitrogen), Alexa Fluor 488 Goat anti-Guinea Pig IgG(H+L) (#A11073, Invitrogen), Alexa Fluor 568 Goat anti-Guinea Pig IgG(H+L) (#A11075, Invitrogen), Alexa Fluor 568 Goat anti-Mouse IgG(H+L) (#A11004, Invitrogen) and Alexa Fluor 633 Goat anti-Mouse IgG(H+L) (#A21050, Invitrogen).

Electron microscopy

Drosophila tissues were fixed in 4% formaldehyde in PBS and stored at 4°C until preparation by high-pressure freezing (HPF) and freeze-substitution (FS) (Buser & Drubin, 2013; Buser & Walther, 2008). Tissues were cryoprotected in 2.3 M sucrose for 45 minutes, transferred to 200 µm deep planchettes and high-pressure frozen in an EMPact2 with RTS (Leica, Vienna, Austria). FS was carried out in an AFS2 (Leica, Vienna, Austria) in methanol containing 5% water, 0.05% glutaraldehyde and 0.1% uranyl acetate (-90 °C, 3 h; -90 to -80 °C, 10 h; -80 °C, 4 h; -80 to 4 °C, 24 h). Samples were washed once in methanol containing 5% water, infiltrated with hard grade LR White (Electron Microscopy Sciences, Hatfield, PA, USA) at 4 °C ([LR White] : [methanol containing 5% water] 1:1, 24 h; 100% LR White, 3x 24 h) and polymerized in a fresh change of LR

White using a Pelco BioWave (Ted Pella, Inc., Redding, CA, USA) set to 750 W, 95 °C for 45 minutes.

60 nm thin sections (UCT ultramicrotome, Leica, Vienna, Austria) were picked up on formvar-coated 50 mesh copper grids. The sections were blocked for 3 minutes in blocking buffer (PBS with 0.5% bovine serum albumin, which was used for all antibody dilutions), incubated in anti-GFP antibody (1:500, Aveslab #1020) for 5 minutes, washed 3 times in blocking buffer, incubated in rabbit anti chicken antibody (1:50, MP Biomedicals #55302) for 5 minutes, washed 3 times on blocking buffer, incubated on protein A - 5nm gold (1:50, Utrecht, Netherlands), and washed 3 times in PBS and 3 times in distilled water. The sections were stained in uranyl acetate or uranyl acetate and Reynolds lead citrate depending on the desired contrast and imaged at 80 kV in a Zeiss EM10C (Zeiss, Oberkochen, Germany) using a CCD camera (Gatan, Pleasanton, CA, USA).

Labeling density was estimated using stereological methods (Griffiths & Hoppeler, 1986). Cross-sections through boutons were recorded and the following parameters were measured: total image area, total number of gold particles, number of visible dense core vesicles (DCV), number of gold particles within a 50 nm radius of the DCV center, bouton area (grid intersection estimate), gold within the bouton cytoplasm, gold within 20 nm of the bouton plasma membrane, gold outside of the bouton (mainly sER). Background labeling was estimated using internal controls (labeling on blank resin and on muscle fibers) and a biological control (non-GFP expressing genotype). Occasional obvious, large gold aggregates were disregarded. Background was consistently below 0.6 gold/ μm^2 in independently repeated labeling experiments.

Electrical Stimulation

The dissection of third-instar larvae was performed in zero-calcium HL3 saline. The CNS was removed to avoid spontaneous motor neuron activity. To minimize muscle contraction induced by electrical stimulation of motor neurons, the larval body walls were slightly stretched and incubated in HL3 saline supplemented with 10 mM glutamate for 5 mins after dissection to desensitize postsynaptic glutamate receptors. Samples were then shifted to HL3 saline containing 1mM glutamate and 1.5mM Ca^{2+} . Motor nerves were sucked into a glass micropipette with a stimulation electrode. In Figure 2 and Figure 3, to induce maximum dense core vesicle release at type III motor neuron terminals, 4 repetitive bursts (70 Hz stimulation for 18-20s with pulse width of 1ms) with intervals of 40-42s were programmed and triggered with a Master-9 stimulator (A.M.P.I., Israel) connected to an iso-flex pulse stimulator (A.M.P.I., Israel). The stimulation intensity was tested and set to double the intensity required to induce muscle contraction by a single pulse stimulation.

In Figure 4, stimulation trials were delivered with the same duration, but with a series of frequencies spanning 1 Hz to 70 Hz.

Calcium imaging

A Nikon A1R confocal microscope with resonant scanner and NIS Element software were used to acquire live Ca^{2+} imaging on third instar larvae, bathed with 1 mM glutamate added in 1.5 mM Ca^{2+} HL3 saline. Type III motor neuron terminals in abdominal segments from A2 to A5 were imaged using a 60x APO 1.4 N.A. water immersion objective with 488 nm excitation laser. A 5-min period was used for time-lapse imaging at a resonance frequency of 1 fps (512 x 512 pixels or 1024 x 1024 pixels), with z-stacks (step length varying from 1 to 1.5 μm) covering the depth of entire type III motor neuron terminals. The repetitive electrical stimulation of 70 Hz was delivered during the

imaging session. Samples with severe muscle contractions were abandoned due to imaging difficulties. Maximum intensity projection (MIP) and image registration were conducted using Image J. Plugins including Image Stabilizer (K. Li, CMU) and Template Matching (Q. Tseng) were used for compensating drifting and correcting movement induced by electrical stimulations. ROIs were manually selected by tracing the outer edge of each neuron based on the baseline fluorescence. If the fluorescence was too weak to trace, we established a reference stack by empirically adjusting the contrast on a duplicate of the raw image stack. We used the reference stack for ROI selection and projected the selected ROIs back onto to the raw image stack for measurement. For frames in which the sample movement could not be automatically corrected, we manually outlined the ROIs used for measurements. Preparations with severe movement or deformation artifacts were abandoned to avoid unreliable measurements. Each ROI represent a traceable neuronal branch except Figure 2—figure supplement 2B, in which the ROIs were further manually partitioned into boutons and IBIs (Inter-Bouton Intervals) based on morphology. Fluorescence change were normalized to the pre-stimulation background except for Figure 3E, for which the data in each trial was normalized to the average $\Delta F/F$ during a 5 seconds period just before stimulation was initiated. No sample size is predetermined based on statistics. Ca^{2+} imaging data were acquired from at least 6 independent NMJs from at least 5 animals.

Statistical Analysis

Data are presented as mean \pm s.e.m. All data analysis was performed with Graphpad Prism 6, Microsoft Excel and custom Matlab codes. Mann-Whitney U test was used for comparison except in Figure 4, where One-sample T test was used for comparison with a specified value (0).

References

- Ales, E., Tabares, L., Poyato, J. M., Valero, V., Lindau, M., & Alvarez de Toledo, G. (1999). High calcium concentrations shift the mode of exocytosis to the kiss-and-run mechanism. *Nat Cell Biol*, *1*(1), 40-44. <https://doi.org/10.1038/9012>
- Barg, S., Olofsson, C. S., Schriever-Abeln, J., Wendt, A., Gebre-Medhin, S., Renstrom, E., & Rorsman, P. (2002). Delay between fusion pore opening and peptide release from large dense-core vesicles in neuroendocrine cells. *Neuron*, *33*(2), 287-299. [https://doi.org/10.1016/S0896-6273\(02\)00563-9](https://doi.org/10.1016/S0896-6273(02)00563-9)
- Bargmann, C. I., & Marder, E. (2013). From the connectome to brain function. *Nature Methods*, *10*(6), 483-490. <https://doi.org/10.1038/Nmeth.2451>
- Barykina, N. V., Subach, O. M., Doronin, D. A., Sotskov, V. P., Roshchina, M. A., Kunitsyna, T. A., Malyshev, A. Y., Smirnov, I. V., Azieva, A. M., Sokolov, I. S., Piatkevich, K. D., Burtsev, M. S., Varizhuk, A. M., Pozmogova, G. E., Anokhin, K. V., Subach, F. V., & Enikolopov, G. N. (2016). A new design for a green calcium indicator with a smaller size and a reduced number of calcium-binding sites. *Sci Rep*, *6*, 34447. <https://doi.org/10.1038/srep34447>
- Burke, N. V., Han, W. P., Li, D. Q., Takimoto, K., Watkins, S. C., & Levitan, E. S. (1997). Neuronal peptide release is limited by secretory granule mobility. *Neuron*, *19*(5), 1095-1102. [https://doi.org/10.1016/S0896-6273\(00\)80400-6](https://doi.org/10.1016/S0896-6273(00)80400-6)
- Buser, C., & Drubin, D. G. (2013). Ultrastructural imaging of endocytic sites in *Saccharomyces cerevisiae* by transmission electron microscopy and immunolabeling. *Microsc Microanal*, *19*(2), 381-392. <https://doi.org/10.1017/S1431927612014304>
- Buser, C., & Walther, P. (2008). Freeze-substitution: the addition of water to polar solvents enhances the retention of structure and acts at temperatures around -60 degrees C. *J Microsc*, *230*(Pt 2), 268-277. <https://doi.org/10.1111/j.1365-2818.2008.01984.x>
- Chen, T. W., Wardill, T. J., Sun, Y., Pulver, S. R., Renninger, S. L., Baohan, A., Schreiter, E. R., Kerr, R. A., Orger, M. B., Jayaraman, V., Looger, L. L., Svoboda, K., & Kim, D. S. (2013). Ultrasensitive fluorescent proteins for imaging neuronal activity. *Nature*, *499*(7458), 295-300. <https://doi.org/10.1038/nature12354>
- Fremeau, R. T., Troyer, M. D., Pahner, I., Nygaard, G. O., Tran, C. H., Reimer, R. J., Bellocchio, E. E., Fortin, D., Storm-Mathisen, J., & Edwards, R. H. (2001). The expression of vesicular glutamate transporters defines two classes of excitatory synapse. *Neuron*, *31*(2), 247-260. [https://doi.org/10.1016/S0896-6273\(01\)00344-0](https://doi.org/10.1016/S0896-6273(01)00344-0)
- Goel, P., & Dickman, D. (2018). Distinct homeostatic modulations stabilize reduced postsynaptic receptivity in response to presynaptic DLK signaling. *Nat Commun*, *9*(1), 1856. <https://doi.org/10.1038/s41467-018-04270-0>
- Gorczyca, M., & Budnik, V. (2006). Anatomy of the Larval Body Wall Muscles and NMJs in the third instar larval stage. *The Fly Neuromuscular Junction: Structure and Function*, *75*, 367.
- Griffiths, G., & Hoppeler, H. (1986). Quantitation in immunocytochemistry: correlation of immunogold labeling to absolute number of membrane antigens. *Journal of Histochemistry & Cytochemistry*, *34*(11), 1389-1398.
- Hentze, J. L., Carlsson, M. A., Kondo, S., Nassel, D. R., & Rewitz, K. F. (2015). The Neuropeptide Allatostatin A Regulates Metabolism and Feeding Decisions in *Drosophila*. *Sci Rep*, *5*, 11680. <https://doi.org/10.1038/srep11680>

- Hokfelt, T., Broberger, C., Xu, Z. Q., Sergeev, V., Ubink, R., & Diez, M. (2000). Neuropeptides--an overview. *Neuropharmacology*, *39*(8), 1337-1356.
- Hoopfer, E. D., Jung, Y., Inagaki, H. K., Rubin, G. M., & Anderson, D. J. (2015). P1 interneurons promote a persistent internal state that enhances inter-male aggression in *Drosophila*. *Elife*, *4*. <https://doi.org/10.7554/eLife.11346>
- Insel, T. R., & Young, L. J. (2000). Neuropeptides and the evolution of social behavior. *Curr Opin Neurobiol*, *10*(6), 784-789.
- Kempf, C., Staudt, T., Bingen, P., Horstmann, H., Engelhardt, J., Hell, S. W., & Kuner, T. (2013). Tissue Multicolor STED Nanoscopy of Presynaptic Proteins in the Calyx of Held. *Plos One*, *8*(4). <https://doi.org/ARTN e6289310.1371/journal.pone.0062893>
- Kendrick, K. M. (1990). Microdialysis measurement of in vivo neuropeptide release. *J Neurosci Methods*, *34*(1-3), 35-46.
- Koon, A. C., & Budnik, V. (2012). Inhibitory control of synaptic and behavioral plasticity by octopaminergic signaling. *J Neurosci*, *32*(18), 6312-6322. <https://doi.org/10.1523/JNEUROSCI.6517-11.2012>
- Levitán, E. S., Lanni, F., & Shakiryanova, D. (2007). In vivo imaging of vesicle motion and release at the *Drosophila* neuromuscular junction. *Nat Protoc*, *2*(5), 1117-1125. <https://doi.org/10.1038/nprot.2007.142>
- Lin, M. Z., & Schnitzer, M. J. (2016). Genetically encoded indicators of neuronal activity. *Nat Neurosci*, *19*(9), 1142-1153. <https://doi.org/10.1038/nn.4359>
- Littleton, J. T., Bellen, H. J., & Perin, M. S. (1993). Expression of synaptotagmin in *Drosophila* reveals transport and localization of synaptic vesicles to the synapse. *Development*, *118*(4), 1077-1088.
- Loveall, B. J., & Deitcher, D. L. (2010). The essential role of bursicon during *Drosophila* development. *BMC Dev Biol*, *10*, 92. <https://doi.org/10.1186/1471-213X-10-92>
- McNabb, S. L., & Truman, J. W. (2008). Light and peptidergic eclosion hormone neurons stimulate a rapid eclosion response that masks circadian emergence in *Drosophila*. *Journal of Experimental Biology*, *211*(14), 2263-2274. <https://doi.org/10.1242/jeb.015818>
- Menon, K. P., Carrillo, R. A., & Zinn, K. (2013). Development and plasticity of the *Drosophila* larval neuromuscular junction. *Wiley Interdiscip Rev Dev Biol*, *2*(5), 647-670. <https://doi.org/10.1002/wdev.108>
- Miesenbock, G., De Angelis, D. A., & Rothman, J. E. (1998). Visualizing secretion and synaptic transmission with pH-sensitive green fluorescent proteins. *Nature*, *394*(6689), 192-195. <https://doi.org/10.1038/28190>
- Mitchell, K. J., Pinton, P., Varadi, A., Tacchetti, C., Ainscow, E. K., Pozzan, T., Rizzuto, R., & Rutter, G. A. (2001). Dense core secretory vesicles revealed as a dynamic Ca²⁺ store in neuroendocrine cells with a vesicle-associated membrane protein aequorin chimera. *Journal of Cell Biology*, *155*(1), 41-51. <https://doi.org/10.1083/jcb.200103145>
- Nassel, D. R., & Winther, A. M. (2010). *Drosophila* neuropeptides in regulation of physiology and behavior. *Prog Neurobiol*, *92*(1), 42-104. <https://doi.org/10.1016/j.pneurobio.2010.04.010>
- Pfeiffer, B. D., Ngo, T. T. B., Hibbard, K. L., Murphy, C., Jenett, A., Truman, J. W., & Rubin, G. M. (2010). Refinement of Tools for Targeted Gene Expression in *Drosophila*. *Genetics*, *186*(2), 735-U488. <https://doi.org/10.1534/genetics.110.119917>
- Rao, S., Lang, C., Levitan, E. S., & Deitcher, D. L. (2001). Visualization of neuropeptide expression, transport, and exocytosis in *Drosophila melanogaster*. *J Neurobiol*, *49*(3), 159-172.

- Schaible, H. G., Jarrott, B., Hope, P. J., & Duggan, A. W. (1990). Release of immunoreactive substance P in the spinal cord during development of acute arthritis in the knee joint of the cat: a study with antibody microprobes. *Brain Res*, *529*(1-2), 214-223.
- Shakiryanova, D., Tully, A., & Levitan, E. S. (2006). Activity-dependent synaptic capture of transiting peptidergic vesicles. *Nat Neurosci*, *9*(7), 896-900. <https://doi.org/10.1038/nn1719>
- Sturman, D. A., Shakiryanova, D., Hewes, R. S., Deitcher, D. L., & Levitan, E. S. (2006). Nearly neutral secretory vesicles in *Drosophila* nerve terminals. *Biophys J*, *90*(6), L45-47. <https://doi.org/10.1529/biophysj.106.080978>
- Sweeney, S. T., Broadie, K., Keane, J., Niemann, H., & O'Kane, C. J. (1995). Targeted expression of tetanus toxin light chain in *Drosophila* specifically eliminates synaptic transmission and causes behavioral defects. *Neuron*, *14*(2), 341-351.
- Taghert, P. H., & Veenstra, J. A. (2003). *Drosophila* neuropeptide signaling. *Adv Genet*, *49*, 1-65.
- Tian, L., Hires, S. A., & Looger, L. L. (2012). Imaging neuronal activity with genetically encoded calcium indicators. *Cold Spring Harb Protoc*, *2012*(6), 647-656. <https://doi.org/10.1101/pdb.top069609>
- Umezaki, Y., Yasuyama, K., Nakagoshi, H., & Tomioka, K. (2011). Blocking synaptic transmission with tetanus toxin light chain reveals modes of neurotransmission in the PDF-positive circadian clock neurons of *Drosophila melanogaster*. *J Insect Physiol*, *57*(9), 1290-1299. <https://doi.org/10.1016/j.jinsphys.2011.06.004>
- van den Pol, A. N. (2012). Neuropeptide transmission in brain circuits. *Neuron*, *76*(1), 98-115. <https://doi.org/10.1016/j.neuron.2012.09.014>
- Winther, A. M. E., Siviter, R. J., Isaac, R. E., Predel, R., & Nassel, D. R. (2003). Neuronal expression of tachykinin-related peptides and gene transcript during postembryonic development of *Drosophila*. *Journal of Comparative Neurology*, *464*(2), 180-196. <https://doi.org/10.1002/cne.10790>
- Wong, M. Y., Cavolo, S. L., & Levitan, E. S. (2015). Synaptic neuropeptide release by dynamin-dependent partial release from circulating vesicles. *Mol Biol Cell*, *26*(13), 2466-2474. <https://doi.org/10.1091/mbc.E15-01-0002>
- Xia, X., Lessmann, V., & Martin, T. F. (2009). Imaging of evoked dense-core-vesicle exocytosis in hippocampal neurons reveals long latencies and kiss-and-run fusion events. *J Cell Sci*, *75*-82. <https://doi.org/10.1242/jcs.034603>
- Xu, T., Binz, T., Niemann, H., & Neher, E. (1998). Multiple kinetic components of exocytosis distinguished by neurotoxin sensitivity. *Nat Neurosci*, *1*(3), 192-200. <https://doi.org/10.1038/642>
- Xu, T., & Xu, P. (2008). Differential Regulation of Small Clear Vesicles and Large Dense-Core Vesicles. In Z.-W. Wang (Ed.), *Molecular Mechanisms of Neurotransmitter Release* (pp. 327-339). Humana Press. https://doi.org/10.1007/978-1-59745-481-0_16
- Zandawala, M., Yurgel, M. E., Texada, M. J., Liao, S., Rewitz, K. F., Keene, A. C., & Nassel, D. R. (2018). Modulation of *Drosophila* post-feeding physiology and behavior by the neuropeptide leucokinin. *PLoS Genet*, *14*(11), e1007767. <https://doi.org/10.1371/journal.pgen.1007767>
- Zhu, D., Zhou, W., Liang, T., Yang, F., Zhang, R. Y., Wu, Z. X., & Xu, T. (2007). Synaptotagmin I and IX function redundantly in controlling fusion pore of large dense core vesicles. *Biochem Biophys Res Commun*, *361*(4), 922-927. <https://doi.org/10.1016/j.bbrc.2007.07.083>